Real-Time Motion Compensation, Image Formation and Image Enhancement of Moving Targets in ISAR and SAR Using S-method Based Approach

Thayananthan Thayaparan, LJubiša Stankovic, Chris Wernik, Miloš Dakovic

Abstract— **The commonly used technique for ISAR/SAR signal analysis is a two dimensional Fourier transform, which results in an image of the target's reflectivity mapped onto a range and cross-range plane. However, in cases where the line-of-sight projections of the target's point velocities change or there is uncompensated movement within the coherent integration time, the Fourier transform produces blurred images. For target recognition applications, mainly those in military surveillance and reconnaissance operations, a blurred ISAR image has to be refocused quickly so that it can be used for real-time target identification. Two standard techniques used for improvement of blurred ISAR images are motion compensation and the use of quadratic time-frequency representations. Both are computationally intensive. In this paper, we present an effective quadratic time-frequency representation, the S-method. This approach performs better than the Fourier transform method by drastically improving images of fast manoeuvring targets and by increasing the SNR in both low and high noise environments. These advantages are a result of the S-method's ability to automatically compensate for quadratic and all even higher-order phase terms. Thus, targets with constant acceleration will undergo full motion compensation and their point-scatterers will each be localized. It should be noted that the source of the quadratic term can come from not only acceleration, but also non-uniform rotational motion and the cosine term in wide-angle imaging. The method is also computationally simple, requiring only slight modifications to the existing Fourier transform based algorithm. The effectiveness of the S-method is demonstrated through application to simulated and experimental data sets.**

IET Signal Processing, Vol. 2, No. 3, Aug. 2008.

I. Introduction

Inverse synthetic aperture radar (ISAR) is a powerful signal processing technique that can provide a two-dimensional image of an area or target of interest. Being radar based, this imaging technique can be employed in all weather and day/night conditions. ISAR images are obtained by coherently processing the received radar echoes of the transmitted pulses. Commonly, the ISAR image is characterized by high resolution along both the range and cross range dimensions. High resolution in the range dimension is achieved by means of large bandwidth pulses, whereas high cross-range resolution is obtained by exploiting a synthetic aperture technique. In ISAR, the synthetic aperture can be generated by motion of the target as well as by motion of the radar platform. In contrast, the related imaging technique of synthetic aperture radar (SAR) has its synthetic aperture generated by means of radar platform motion only [1], [2].

The inverse synthetic aperture is formed by the coherent integration of signals obtained from the fixed aperture radar as the target translates and rotates "within the radar's beam width", creating the equivalent of a large circular aperture focused at the target's center-of-rotation [3], [4]. The underlying concept in ISAR imaging is to use the Doppler information provided by the different velocities, relative to the radar, of individual scatterers to obtain high cross range resolution. That is, we decompose the target (spatially) into a set

of individual "point" scatterers each of which has a different Doppler velocity represented by Doppler frequency shifts. Thus, the distribution of the target's reflectivity function can be measured by the Doppler spectrum. Typically, the Doppler spectrum is obtained using conventional Fourier transform techniques implemented, computationally, using a fast Fourier transform (FFT) algorithm with the underlying assumption that the Doppler frequency is fixed or is time invariant. In ISAR scenarios, where the target is moving smoothly with respect to the radar and when the coherent integration time (CIT) is short, the Fourier transform represents the most effective solution. Nevertheless, in ISAR scenarios with fast manoeuvring targets or with sea-driven ship motion, the effectiveness of the Fourier approach is limited [1], [5], [6], [7]. For this reason, several other techniques have been proposed.

One proven approach for achieving ISAR motion compensation and focused distorted ISAR images is the adaptive joint time-frequency (AJTF) algorithm [6], [7]. An adaptive time-frequency procedure is used to extract the phases of the prominent point-scatterers on the target. The extracted phase information is then used in conjunction with a prominent point processing (PPP) model to remove higher-order motion errors in the radar data. In this procedure, the phase of the resulting focused image is preserved and the Doppler resolution offered by the full coherent processing interval can be achieved. However, this algorithm is not without significant weaknesses. One of the problems is that the computational burden of the exhaustive search used to extract the motion compensation parameters, limits its usefulness in an operational situation.

Another approach is based on the use of quadratic time-frequency representations [1], [8], [9], [10]. Time-frequency techniques are known to be successful in refocusing blurred ISAR images. This occurs because the images are obtained at a particular instant in time when the target's motion can be considered uniform. However, the data is not collected instantaneously. Consequently, a large number of refocused ISAR images will be generated, spanning the entire CIT. For accurate target recognition, it is imperative to make use of only the best refocused image. It would be very impractical and inefficient to examine all of the images produced in order to identify which is the best. Such manual inspection, or even with the aid of an automated image searching algorithm, only adds extra complexity to the target recognition process [11]. The basic quadratic time-frequency representation is the Wigner-Ville distribution (WVD). In contrast to the Fourier transform, the WVD can produce a fully concentrated representation only if the signal frequency changes are linear. However, the WVD suffers from cross-terms if there is more than one point-scatterer at the same range in ISAR analysis. These were the reasons for introducing other quadratic time-frequency representations, with simplicity, efficiency and reduced interference as essential conditions.

In this paper we propose that the S-method based calculation be used [12], [13], [14]. As with the WVD, the S-method can produce concentrated representations of linear frequency changes and has the added advantage of being cross-term free (or with significantly reduced cross-terms). In contrast to other reduced interference distributions, which are usually derived under the condition that the marginal properties are preserved (what inherently leads to auto-term degradation with respect to the WVD [15]), the S-method is derived with the goal of preserving the same auto-terms as in the WVD, while avoiding cross-terms [16], [17], [18]. In other words, the method automatically compensates for quadratic and all even higher-order terms in phase induced by the target's complex motion, leading to well-focused images. The S-method is also numerically very simple and requires just a few more operations than the standard Fourier transform based algorithm. This method works on the whole set of data and it does not split the ISAR image into a time series of ISAR images, as in the case of common time-frequency techniques. These are significant advantages over other quadratic representations and over linear transforms based on

signal dechirping and multiparameter search procedures.

The objective of this paper is to demonstrate the effectiveness of the S-method for real-time image refocusing using both simulated and experimental targets exhibiting two and three-dimensional motion. Three numerical models were developed to simulate targets with complex rotational motion. This motion is that of in-flight aircraft in that it incorporates changes in pitch, roll and yaw. Experiments were conducted to gather data from a delta-wing shaped apparatus with six corner reflectors. These experiments were carried out in order to study severe distortions in ISAR images. The experimental data are then used for comparing and validating the simulated results. Statistical study of the results and achieved improvements are discussed.

II. Analytic CW Radar Signal Model

For the analytic derivation of the model, consider a continuous wave (CW) radar that transmits a signal in the form of a coherent series of chirps [1]:

$$v_p(t) = \begin{cases} e^{(j\pi B f_r t^2)} & \text{for} \quad 0 \le t \le T_r \\ 0 & \text{otherwise} \end{cases} \qquad (1)$$

where T_r is the repetition time, $f_r = 1/T_r$ is the repetition frequency, and B is the emitted waveform bandwidth.

In one revisit, the transmitted signal consists of M such chirps:

$$v(t) = e^{(-j\omega_0 t)} \sum_{m=0}^{M-1} v_p(t - mT_r) \qquad (2)$$

where ω_0 is the radar operating frequency. The total signal duration is $T_c = MT_r$ and represents the CIT.

Consider a signal of form (2) transmitted toward a target. If the target distance from the radar is d (referred to as range), then the received signal is delayed with respect to the transmitted signal for $t_d = 2d/c$, where c is the velocity of propagation, equal to the speed of light. The phase of the received signal is changed as $\phi = 2kd = 4\pi d/\lambda = 4\pi d f_0/c = 2\omega_0 d/c$.

Thus, the form of the received signal is

$$u(t) = \sigma e^{(j[-\omega_0(t-\frac{2d}{c})])} \sum_{m=0}^{M-1} v_p(t - \frac{2d}{c} - mT_r)$$

where σ is the reflection coefficient. The received signal is mixed (multiplied) with the complex-conjugate of the transmitted signal and shifted in time with a minimal delay T_0. We will assume that a constant distance is properly compensated and that $T_0 = 0$. Without loss of generality, we can consider only one component of the received signal:

$$q(m,t) = \sigma e^{(j\omega_0 \frac{2d}{c})} e^{(-j2\pi B f_r (t - mT_r)\frac{2d}{c})}.$$

A two-dimensional discrete signal is obtained by sampling in time with $t - mT_r = nT_s$

$$q(m,n) = \sigma e^{(j\omega_0 \frac{2d}{c})} e^{(-j2\pi B f_r n T_s \frac{2d}{c})}.$$

III. ISAR Basic Definitions and Model

Inverse synthetic aperture radar (ISAR) is a method for obtaining high resolution of a target based on the change in viewing angle of the target with respect to a fixed radar. An illustration of a target and relevant quantities is shown in Figure 1. Suppose that a target consists of P point scatterers whose locations are (x_p, y_p), $p = 1, 2, ..., P$, in the coordinate system whose center is the center of target rotation. The coordinate in the direction of the radar-target line (range coordinate) is denoted by x_p, while y_p is the coordinate in the normal direction to this line (cross-range coordinate). The target's total movement can be considered as a superposition of both translation and rotation.

Assume that the target moves along a straight line parallel to the ground at a height h, and that its ground distance from radar is z,meaning the range $d = \sqrt{h^2 + z^2}$. From the radar position the target is seen at an angle α, meaning $\sin(\alpha) = h/d$. In the next instant, $t + \Delta t$, the target is moved to the new position corresponding to the ground distance $z + \Delta z$, meaning the range $d = \sqrt{h^2 + (z + \Delta z)^2}$, and it is seen from the radar at an angle $\alpha + \Delta\alpha$. Thus, this movement can be considered as a

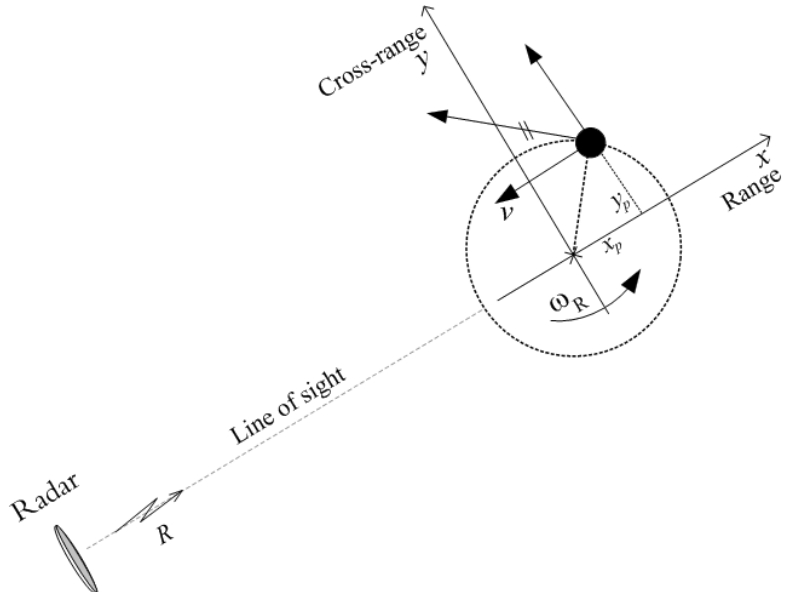

Fig. 1. Illustration of the ISAR principle.

translation for Δd and rotation for $\Delta\alpha$. If the target speed is v_t then $\Delta z = v_t \Delta t$. Since

$$\alpha = \tan^{-1}(\frac{h}{z}) \text{ and } \frac{\partial \alpha}{\partial z} = \frac{-h}{z^2+h^2}$$

we get

$$\Delta\alpha \cong \frac{-h}{z^2+h^2}\Delta z$$

or

$$\Delta\alpha \cong -(\Delta z)h/d^2 = -v_t(\Delta t)h/d^2.$$

During the considered time interval t the point scatterer rotates for $\theta_R(t) = \omega_R t$. The new coordinates of the scatterer are

$$\begin{bmatrix} x'_p \\ y'_p \end{bmatrix} = \begin{bmatrix} \cos(\theta_R(t) & \sin(\theta_R(t)) \\ -\sin(\theta_R(t) & \cos(\theta_R(t)) \end{bmatrix} \begin{bmatrix} x_p \\ y_p \end{bmatrix} \quad (3)$$

The total range position, for small $\theta_R(t) \to 0$, is

$$d(t) = \sqrt{(R+x'_p)^2 + y'^2_p} \cong R + x'_p$$

$$= R + x_p \cos(\theta_R(t)) + y_p \sin(\theta_R(t))$$

$$\cong R + x_p \quad (4)$$

The range contains information about coordinate x_p, since for $\theta_R(t) = \omega_R t \to 0$ we get, $\cos(\theta_R(t)) \to 1$, $\sin(\theta_R(t)) \to \theta_R(t)$ and $d(t) \cong R + x_p + y_p \omega_R t$.

The Doppler shift is proportional to the velocity in the direction of the line-of-sight (LOS):

$$\Delta\omega_d \cong \frac{2\omega_0}{c}\frac{d}{dt}[d(t)] =$$

$$= \frac{2\omega_0}{c}\frac{d}{dt}[R + x_p \cos(\theta_R(t)) + y_p \sin(\theta_R(t))]$$

For $\theta_R(t) = \omega_R t \to 0$ again $d(t) \cong R + x_p + y_p \omega_R t$. Note that here we must not neglect the term $y_p \omega_R t$ since it is multiplied by a large number $2\omega_0/c$ in defining the phase of $\exp(j2\omega_0 d/c)$. Thus,

$$\Delta\omega_d = \frac{2\omega_0}{c} y_p \omega_R \sim y_p$$

assuming, in addition to the above approximations, that the translation is compensated, i.e., $R(t) = R$.

A. Non-uniform Motion

In general, target motion over M chirps in one revisit cannot be considered as linear with velocity $v = y_p \omega_R$. Even in the simplest case when the target rotates with a constant angular velocity ω_R, for a longer period of time,

the line-of-sight projection of the point scatterer velocity is

$$v_s(t) = \omega_R r_p \sin(\omega_R t)$$

where $r_p = \sqrt{x_p^2 + y_p^2}$. Obviously, from the same figure we have

$$\begin{aligned} y_p &= r_p \sin(\omega_R t) \\ x_p &= r_p \cos(\omega_R t). \end{aligned}$$

Thus, for the interval $[t, t+\Delta t]$, the cross-range coordinate moves within

$$[y_p, y_p + \Delta y_p] =$$

$$= [r_p \sin(\omega_R t), r_p \sin(\omega_R (t+\Delta t))]$$

where

$$\begin{aligned} y_p + \Delta y_p &= r_p \sin(\omega_R (t+\Delta t)) \\ &= r_p \sin(\omega_R t)\cos(\omega_R \Delta t) \\ &\quad + r_p \cos(\omega_R t)\sin(\omega_R \Delta t) \\ &= y_p \cos(\omega_R \Delta t) + x_p \sin(\omega_R \Delta t) \end{aligned}$$

For small $\omega_R \Delta t$ we can write:

$$\begin{aligned} y_p + \Delta y_p &\cong y_p + x_p \omega_R \Delta t - y_p \frac{(\omega_R \Delta t)^2}{2} \\ &\quad - x_p \frac{(\omega_R \Delta t)^3}{6} + ... \\ &\cong y_p + x_p \omega_R \Delta t \end{aligned} \quad (5)$$

Then, the LOS projection of the velocity changes within

$$[v_s(t), v_s(t) + \Delta v_s(t)] =$$

$$= [\omega_R y_p, \omega_R y_p + x_p \omega_R \Delta t] \quad (6)$$

meaning that for intervals, such that $x_p \omega_R \Delta t$ can not be neglected with respect to y_p, the Doppler shift is a linear function of time with rate $x_p \omega_R$. Thus, instead of the delta pulse concentrated at one frequency, corresponding to $\omega_R y_p$ we will obtain a function corresponding to a LFM signal whose instantaneous frequency changes according to equation (6). The same holds for the range coordinate x_p.

If the assumption about small enough $\omega_R \Delta t$ does not hold then the changes of instantaneous frequency are not linear. In addition, if ω_R is not constant, then high nonlinearity in the instantaneous frequency can be expected, (5). The result is that, instead of having a 2D Fourier transform concentrated at the point corresponding to (x_p, y_p), we will obtain a spread Fourier transform, meaning a blurred radar image.

IV. Fourier Transform in ISAR

The two-dimensional (2D) Fourier transform of the received signal is

$$Q(m', n') =$$

$$= \sum_{m=0}^{M-1} \sum_{n=0}^{N-1} q(m,n) e^{(-j[2\pi m m'/M + 2\pi n n'/N])}$$

where time is discretized such that $t - mT_r = nT_s$. The periodogram

$$P(m', n') = |Q(m', n')|^2$$

represents an ISAR image.

In order to analyze cross-range nonstationarities in the Fourier transform, we consider only the Doppler component part of the received signal (the p-th point scatterer), as it is usually done in the literature on ISAR,

$$\begin{aligned} e_p(t) &= \sigma_p e^{(j\frac{2\omega_0}{c} d_p(t))} \\ &= \sigma_p e^{(j\frac{2\omega_0}{c}(x_p \cos(\theta_R(t)) + y_p \sin(\theta_R(t))))}. \end{aligned} \quad (7)$$

The Fourier transform of $e_p(t)$ produces

$$E_p(\omega) = \int_{-Tc/2}^{T_c/2} e_p(t) e^{(-j\omega t)} dt$$

$$= \int_{-\infty}^{\infty} w(t) e_p(t) e^{(-j\omega t)} dt,$$

where $w(t)$ is the window defining the considered time interval (CIT). In order to simplify the notation we will just omit the index p.

For time-varying $d(t)$ we can write a Taylor series expansion of $d(t)$ around $t = 0$:

$$\begin{aligned} d(t) &= d_0 + d'(0)t + \frac{1}{2} d''(0) t^2 + ... \\ &= \sum_{n=0}^{\infty} \frac{1}{n!} d^{(n)}(0) t^n, \end{aligned} \quad (8)$$

where $d^{(n)}(0)$ is the $n-$th derivative of the distance at $t=0$ and $2\omega_0 d'(0)/c = \Delta\omega_d$.

Fourier transform (FT) of (7) with (8) is of the form

$$E(\omega) = \\ = \int_{-\infty}^{\infty} w(t) e^{(j\frac{2\omega_0}{c}\sum_{n=0}^{\infty}\frac{1}{n!}d^{(n)}(0)t^n)} e^{(-j\omega t)} dt \\ = \int_{-\infty}^{\infty} w(t) e^{\left(j\frac{2\omega_0}{c}\left\{[d(0)+d'(0)t+\sum_{n=2}^{\infty}\frac{1}{n!}d^{(n)}(0)t^n\right\}\right)} \\ \times e^{(-j\omega t)} dt \quad (9)$$

Now, by omitting the constant term $d(0)$ and shifting $2\omega_0 d'(0)/c = \Delta\omega_d$ into the second exponential term we get

$$E(\omega) = \int_{-\infty}^{\infty} w(t) e^{(j\frac{2\omega_0}{c}\sum_{n=2}^{\infty}\frac{1}{n!}d^{(n)}(0)t^n)} \\ \times e^{(-j[\omega-2\omega_0 d'(0)/c]t)} dt. \quad (10)$$

This is a Fourier transform of a product of the window $w(t)$ and the first exponential function, calculated at the frequency $\omega - 2\omega_0 d'(0)/c = \omega - \Delta\omega_d$. The Fourier transform of a product of two functions is equal to the convolution of their Fourier transforms, resulting in

$$E(\omega) = \\ = W(\omega-\Delta\omega_d) *_\omega FT\left[e^{(j\frac{2\omega_0}{c}\sum_{n=2}^{\infty}\frac{1}{n!}d^{(n)}(0)t^n)}\right],$$

where $*_\omega$ denotes convolution in frequency. Thus, the Fourier transform is located at and around the Doppler shift $\omega = \Delta\omega_d$. It is spread by the factor

$$S_{spread}(\omega) = FT\left[e^{(j\frac{2\omega_0}{c}\sum_{n=2}^{\infty}\frac{1}{n!}d^{(n)}(0)t^n)}\right].$$

This factor depends on the derivatives of the distance, starting from the second order (first order derivative of the Doppler shift), i.e., the spread factor depends on

$$s_f(t) = \frac{1}{2}d''(0)t^2 + \frac{1}{6}d'''(0)t^3 + ...$$

It can significantly degrade the periodogram image:

$$P(\omega) = |E(\omega)|^2.$$

V. S-method Based Improvement of the Radar Images

In this section we will present a method for improvement of images blurred due to the long CIT and/or nonuniform movement. Instead of using the Fourier transform (periodogram), we use the S-method defined by [16], [18]

$$SM(\omega) = \frac{1}{\pi}\int_{-\infty}^{\infty} E(\omega+\theta)E^*(\omega-\theta)d\theta. \quad (11)$$

This method can improve the image concentration in a numerically very simple and efficient way. Namely, by replacing $E(\omega)$ from (IV) into (11) we get

$$SM(\omega) = \frac{1}{\pi}\int_{-\infty}^{\infty}\int_{-\infty}^{\infty}\int_{-\infty}^{\infty} w(t_1)w^*(t_2) \\ \times e^{(j\frac{2\omega_0}{c}\sum_{n=0}^{\infty}\frac{1}{n!}d^{(n)}(0)t_1^n)} e^{(-j\frac{2\omega_0}{c}\sum_{n=0}^{\infty}\frac{1}{n!}d^{(n)}(0)t_2^n)} \\ \times e^{(-j(\omega+\theta)t_1)} e^{(j(\omega-\theta)t_2)} dt_1 dt_2 d\theta.$$

The part of integrand depending on θ is $\exp(-j\theta(t_1+t_2))$. Integration over θ results in $2\pi\delta(t_1+t_2)$. Integration of a function $g(t_1)g(t_2)\delta(t_1+t_2)$ over t_1 results in the function $g(t)g(-t)$ for $t_1 = -t_2 = t$. From the previous equation it means that we obtain

$$SM(\omega) = 2\int_{-\infty}^{\infty} w(t)w^*(-t) \\ \times e^{(j\frac{2\omega_0}{c}\sum_{n=0}^{\infty}\frac{1}{n!}d^{(n)}(0)(t^n-(-t)^n))} e^{(-j2\omega t)} dt \\ = W_e(\omega-\Delta\omega_d) *_\omega FT\left[e^{(j\frac{2\omega_0}{c}\frac{1}{3!}d'''(0)t^3+...)}\right]$$

where similar calculations as in (IV)-(10) are performed.

The S-method based image is located at the same position in Doppler space as the Fourier transform image, $\omega = \Delta\omega_d$, but with the spreading term

$$S_{spread}(\omega) = FT\left[e^{(j\frac{2\omega_0}{c}(\frac{1}{3!}d'''(0)t^3+...)}\right]$$

Its exponent starts from the third derivative $d'''(0)$,

$$s_f(t) = \frac{1}{6}d'''(0)t^3 + \frac{1}{120}d^{(5)}(0)t^5 + ...$$

This means that the S-method has the ability to automatically compensate for quadratic and all even higher-order terms in phase. Recall that in the Fourier transform based image the spreading terms started from the second derivative $d''(0)$. It means that in the S-method, the points with linear Doppler changes,

$$\frac{2\omega_0}{c}d'(t) = \Delta\omega_d(t) = \Delta\omega_d + at$$

will be fully concentrated without any spread, since here $s_f(t) = 0$. Thus, targets with constant acceleration will undergo full motion compensation and their point-scatterers will each be localized. Note that $W_e(\omega)$ is the Fourier transform of window $w(t/2)w^*(-t/2)$ while $\Delta\omega_d$ without argument denotes the constant part of $\Delta\omega_d(t)$, i.e., $\Delta\omega_d = \Delta\omega_d(0)$. It should also be noted that the source of the quadratic term can come from not only acceleration, but also non-uniform rotational motion and the cosine term in wide-angle imaging.

A. Numerical Implementation

The discrete version of (11) is

$$SM(k) = \sum_{i=-L}^{L} E(k+i)E^*(k-i)$$

$$= |E(k)|^2 + 2\,\mathrm{real}\{\sum_{i=1}^{L} E(k+i)E^*(k-i)\}$$

In theory, L should be such as to provide calculation over the whole frequency range. However since the first term is $|E(k)|^2$, i.e., the periodogram, while the terms $2\,\mathrm{real}\{E(k+i)E^*(k-i)\}$, for $i = 1, 2, ...$, are used to improve the periodogram concentration in the case of time-varying Doppler shift, only a few terms are enough to provide complete integration over the one target point and achieve high resolution. The S-method can be realized in a recursive form, as well. If we denote

$$SM_L(k) = \sum_{i=-L}^{L} E(k+i)E^*(k-i)$$

then

$$SM_L(k) = SM_{L-1}(k) + 2\,\mathrm{real}\{E(k+L)E^*(k-L)\}, \qquad (12)$$

with $SM_0(k) = |E(k)|^2$ being the standard Fourier transform based representation.

Therefore, the S-method improvement can be achieved starting with the radar image, with additional simple matrix calculation according to (12). It is obvious that the total calculation complexity, for adding one more term to the existing Fourier transform image or to the existing S-method image, is one addition and one multiplication, for each point. For each next L+1, just one more multiplication and addition is needed. In theory, when L is equal to the width of auto-term (width of the blurred point in the radar image) the radar image is completely focused and there is no need to further increase L. In practice, it means just to take 2 to 6 terms for L. Note that it is also possible to use S-method with self-adaptive number of samples. A very detailed analysis of calculation complexity may be also found in [16].

Here, we applied a window $w(m)$, and calculated

$$Q(m', n') = \sum_{m=0}^{M-1}\sum_{n=0}^{N-1} w(m)q(m,n) \times e^{(-j[2\pi mm'/M + 2\pi nn'/N])}.$$

In examples provided, we used such a window that $w^2(m)$ is the Hanning window ($w(m)$ is then close to the rectangular window form).

B. Analysis of the Proposed Improvement

B.1 Multipoint Target in the Same Range Bin

If the target contains more than one point-scatterer at a given range bin then the signal is of the form

$$e(t) = \sum_{p=1}^{Q} e_p(t) = \sum_{p=1}^{Q} \sigma_p e^{(j\frac{2\omega_0}{c}d_p(t))}.$$

The S-method is then

$$SM(\omega) = \sum_{p=1}^{Q}\sum_{q=1}^{Q}\int_{-\infty}^{\infty} E_p(\omega+\theta)E_q^*(\omega-\theta)d\theta =$$

$$= \sum_{p=1}^{Q}\int_{-\infty}^{\infty} E_p(\omega+\theta)E_p^*(\omega-\theta)d\theta$$

$$+\sum_{\substack{p=1\\p\neq q}}^{Q}\sum_{q=1}^{Q}\int_{-\infty}^{\infty} E_p(\omega+\theta)E_q^*(\omega-\theta)d\theta.$$

The first sum represents target points, individually, i.e., auto-terms. Assume that the width of the Fourier transform $E_p(\omega)$ around $\Delta\omega_{dp}$ is $2W_P$ (for Doppler shift $\Delta\omega_d(t) = \Delta\omega_d + at$ and CIT T_c the width is approximately $2W_P = aT_c$). The value of (11) over θ within $-W_P \leq \theta \leq W_P$ will be the same with respect to these terms as integration from $-\infty$ to ∞. Thus, the S-method can be calculated as

$$SM(\omega) = \int_{-\infty}^{\infty} P(\theta)E(\omega+\theta)E^*(\omega-\theta)d\theta$$

where $P(\theta)$ is the rectangular window of the width defined by $-W_P \leq \theta \leq W_P$.

The second sum in $SM(\omega)$ represents "cross-terms". Since $E_p(\omega+\theta)$ is located around $\omega+\theta = \Delta\omega_{dp}$ and $E_q(\omega+\theta)$ is located around $\omega-\theta = \Delta\omega_{dq}$, if we restrict the integration over θ to $|\theta| < W_P$ then $E_p(\omega+\theta)E_q^*(\omega-\theta) = 0$ if $|\Delta\omega_{dp} - \Delta\omega_{dq}| > 2W_P$.

It means that we will be able to obtain fully concentrated point-scatterer locations as in the WVD, without cross-terms, if the above conditions are satisfied. If the conditions are not satisfied for some components and range bins, the cross-terms will start appearing, but only for those components and range bins. Still, cross-terms will be reduced with respect to the WVD.

In radar images, L samples in $P(\theta)$ on each side of the θ origin, is equivalent to taking $2L$ cross-range bins and focusing on a cross-range value of $2LR_{cross-range} = 2L\pi c/(\omega_0 T_c \omega_R)$. For example, if $R_{cross-range} = 0.1$m, by taking $L = 3$ in the S-method the cross-terms would start appearing only when the distance in cross-range is smaller than 0.6m for the same range. Another way to deal with cases where components are too close or partially overlap in cross-range is by using varying values of L, as presented in [17]. Then, the cross-terms will be completely avoided in the cases of nonoverlapping auto-terms.

B.2 Accuracy Analysis of Noisy Signals

Consider a reflected signal with additive noise $\varepsilon(t)$

$$e_p(t) = \sigma_p e^{(j\frac{2\omega_0}{c}d_p(t))} + \varepsilon(t)$$

1. Case with stationary Doppler shift.

When time variations of the Doppler shift within the CIT are very small they can be neglected, $d_p'(0) = \Delta\omega_d$ and $d_p^{(n)}(0) \approx 0$ for $n > 1$, and we can write:

$$E_p(\omega) =$$

$$= \sigma_p W(\omega-\Delta\omega_d) *_\omega FT\left[e^{(j\frac{2\omega_0}{c}\sum_{n=2}^{\infty}\frac{1}{n!}d_p^{(n)}(0)t^n)}\right]$$

$$\cong \sigma_p W(\omega-\Delta\omega_d) \qquad (13)$$

Here, there is no need for any improvement. The Fourier transform and corresponding periodogram is the maximum likelihood (ML) estimate for Gaussian additive noise.

2. Time-varying case when $d_p^{(n)}(0)$ for $n > 1$ can not be neglected.

The Fourier transform of non-noisy signal can be approximated by using the stationary phase method [19], [20] so that

$$E_p(\omega) = \int_{-\infty}^{\infty} w(t)\sigma_p e^{(j\frac{2\omega_0}{c}d_p(t))}e^{(-j\omega t)}dt$$

$$\cong \sigma_p e^{(j\frac{2\omega_0}{c}d_p(t_0)-j\omega t_0)}w(t_0)\sqrt{\frac{2\pi j}{\left|\frac{2\omega_0}{c}d_p''(t_0)\right|}},$$

$$\text{with } \frac{2\omega_0}{c}d_p'(t_0) = \omega.$$

where $w(t)$ is the time window whose width is defined by the CIT. Therefore,

$$|E_p(\omega)|^2 = \sigma_p^2 w^2(t_0)\frac{2\pi}{\left|\frac{2\omega_0}{c}d_p''(t_0)\right|}. \qquad (14)$$

For linear changes of the Doppler frequency shift, i.e., for $\frac{2\omega_0}{c}d_p'(t) = \Delta\omega_d(t) = \Delta\omega_d + at$, we have $\Delta\omega_d + at_0 = \omega$, and

$$|E_p(\omega)|^2 = \sigma_p^2 w^2(\frac{\omega-\Delta\omega_d}{a})\frac{2\pi}{|a|}. \qquad (15)$$

Thus, the amplitude of $|E_p(\omega)|^2$ does not increase with the window length, as in the case of a stationary Doppler shift, but it is defined by the window's time domain maximal value, usually $w(0) = 1$. The width of $|E_p(\omega)|^2$, denoted by W_p, represent's a measure of blurring, and is defined by the window (CIT) width $-T_c/2 \leq (\omega - \Delta\omega_d)/a \leq T_c/2$ or $W_p = aT_c$. Note that not only the radar image will be blurred, but also strong noise can degrade its performance. Doppler shift (cross-range) detection is directly related to the maximum of $|E_p(\omega)|^2$ detection.

Small noise analysis: The bias of the Doppler shift is defined as a difference of its true value and the position of maxima in the Fourier transform.. Maxima are defined by the auto-term functions (14). For example, $w^2(t_0)$ with $\frac{2\omega_0}{c}d'_p(t_0) = \omega$ reaches its maximum at the solution of $d'^{-1}_p(\frac{c\omega}{2\omega_0}) = 0$, where $d'^{-1}_p(\omega)$ denotes inverse function of $d'_p(t)$, $d'_p(d'^{-1}_p(\omega)) = \omega$. Doppler shift is unbiased for $\frac{2\omega_0}{c}d'_p(t) = \Delta\omega_d(t) = \Delta\omega_d + at$, as it can be seen from (15). If the third order derivative cannot be neglected, i.e., $\frac{2\omega_0}{c}d'_p(t) = \Delta\omega_d(t) = \Delta\omega_d + at + bt^2/2$, then the bias is proportional to b, [21]

$$bias(\Delta\omega_d) = bT_cK_w$$

where K_w is window shape defined constant, $K_w = \mathcal{M}^w_4/(6\mathcal{M}^w_2)$ with

$$\mathcal{M}^w_k = \int_{-T_c/2}^{T_c/2} w(t)t^k dt.$$

For example, for a rectangular window $\mathcal{M}^w_2 = T_c^3/12$.

A small noise component will also cause random variations of maxima around the non-noisy maxima positions. These variations are described by the variance. For a periodogram (15) of a nonstationary signal it reads [21]:

$$var(\Delta\omega_d) = \frac{\sigma^2_\varepsilon}{\sigma^2_p}\frac{\mathcal{M}^{w^2}_2}{4\pi(w^{(2)}(0))^2}T_rT_c^7a^5.$$

The S-method for component with $\frac{2\omega_0}{c}d'_p(t) = \Delta\omega_d(t) = \Delta\omega_d + at$ produces a fully concentrated representation

$$SM_p(\omega) = \sigma^2_pW_e(\omega - \Delta\omega_d).$$

Obviously, in contrast to the Fourier transform based analysis (15), its "concentration" increases with the window length (CIT) value, meaning that it can outperform the Fourier transform based analysis in noisy cases. Variance for the small noise case and a signal of this form is [22]

$$var(\Delta\omega_d) = \frac{\sigma^2_\varepsilon}{2\sigma^2_p}(1 + \frac{\sigma^2_\varepsilon}{2\sigma^2_p})\frac{\mathcal{M}^{w^2}_2}{(\mathcal{M}^w_2)^2}.$$

High noise analysis: When the noise is high then the dominant source of error is in the incorrect detection of maxima, which occurs when some noise values in the radar image are higher than the component values along the auto-terms. A measure of this error is the ratio of the distribution maximum with no noise present to the variance of noise in the periodogram's noisy regions. This SNR ratio for the periodogram [23], [24] is:

$$SNR_{period} = \frac{\left|\max\{|E_p(m')|^2\}_{without\_noise}\right|^2}{var\{|E_p(m')|^2\}_{only\_noise}}.$$

The above expression is a measure of correct and incorrect detection of the target's point-scatterers' positions. If $var\{|E_p(m')|^2\}_{only\_noise}$ is high then there is a large possibility that the detector will detect any arbitrarily positioned point instead of the true signal's non-noisy maximum. For a signal with $\Delta\omega_d(t) = \Delta\omega_d + at$ it reads [23]

$$SNR_{period} = \frac{4\pi^2N^2\sigma^4_p}{(aT_c^2)^2\sigma^4_\varepsilon}.$$

For the S-method, the same analysis leads to [23]

$$SNR_{SM} = \frac{N^2\sigma^4_pC^2_w}{T_c^2(2L+1)\sigma^4_\varepsilon}$$

The maximal ratio of these SNRs for the value of L, such that complete concentration of an auto-term is achieved, is equal to

$$\frac{SNR_{SM}}{SNR_{period}} = \frac{a}{2\pi}C^2_w$$

where $C_w = \int_{-T_c/2}^{T_c/2} w^2(t)dt$. For the Hanning window $w^2(t)$ we get $C_w = T_c/2$ and

$$\frac{SNR_{SM}}{SNR_{period}} = \frac{a}{8\pi}T_c^2. \qquad (16)$$

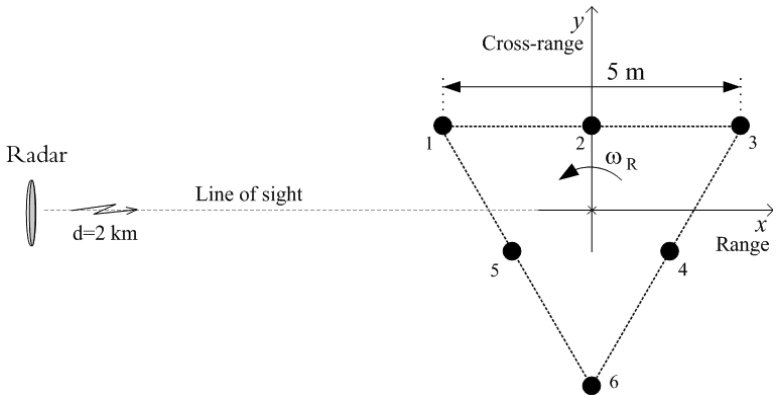

Fig. 2. The two-dimensional radar target model.

Note that in the case of the periodogram, due to its spread, there are several candidates for the maximum at the same auto-term. It means that a high noise level in the periodogram will cause two kinds of errors: 1) A complete miss of the component, when all auto-term values are surpassed by noise, resulting in a higher percentage of missed points, and 2) Variations within the auto-term values, when instead of the correct term, one of the neighboring auto-term values is picked as the maximum, causing higher mean square error (MSE) in the detection of "correct" points. In the S-method, auto-terms are highly concentrated, meaning only one auto-term value exists and that the first kind of error will dominate. It also means that in a comparison, both of these kinds of errors should be taken into account when analyzing statistical data. The described improvement corresponds to the statistical analysis of results presented earlier.

B.3 Application to a Two-Dimensional Target Model

The "setup" in [25], [7] assumes: a high resolution radar operating at the frequency $f_0 = 10.1$ GHz, a bandwidth of linear FM chirps of $B = 300$ MHz, and a pulse repetition frequency $f_r = 1/T_r = 2$ kHz with 2048 pulses in one revisit ($T_c \cong 2$ sec, cases with $T_c \cong 1$ sec and $T_c \cong 4$ sec are also considered). The pulse repetition time is $T_r = 0.5$ ms. The target is at a 2 km distance from the radar, and rotates at $\omega_R = 4^0/\,\mathrm{sec}$. The nonlinear rotation with frequency $\Omega = 0.5$ Hz is superimposed, $\omega_R(t) = \omega_R + A\sin(2\pi\Omega t)$, and amplitude $A = 1.25^0/\,\mathrm{sec}$ corresponds to the total change in angular frequency ω_R for $2.5^0/\,\mathrm{sec}$. Note that here range and cross-range resolutions are $R_{range} = c/(2B) = 0.5$ m, and $R_{cross-range} = \pi c/(\omega_0 T_c \omega_R) = 0.106$ m. Since no translation in the experiment exists, there is no need for translation compensation.

We assume that at $t = 0$ the line connecting points 1, 2 and 3 is parallel to the line-of-sight, as shown in Figure 2. Then at $t = 0$ we have $(x_1, y_1) = (-2.5, 1.44)$, $(x_2, y_2) = (0, 1.44)$, $(x_3, y_3) = (2.5, 1.44)$, $(x_4, y_4) = (1.25, -0.72)$, $(x_5, y_5) = (-1.25, -0.72)$ and $(x_6, y_6) = (0, -2.89)$. All dimensions are in meters. Note again that resolutions in both directions depend on T_c, c and B, but not on T_r, N and M.

The signal model corresponding to one of 6 rotating parts is

$$d_p(t) = R + x_p\cos(\theta_R(t)) + y_p\sin(\theta_R(t))$$

or after distance compensation $d_p(t) = x_p\cos(\theta_R(t)) + y_p\sin(\theta_R(t))$ we have

$$\Delta\omega_d \cong \frac{2\omega_0}{c}\frac{d}{dt}[d_p(t)]$$

$$= \frac{2\omega_0}{c}(-x_p\theta'_R(t)\sin(\theta_R(t)) + y_p\theta'_R(t)\cos(\theta_R(t))) \quad (17)$$

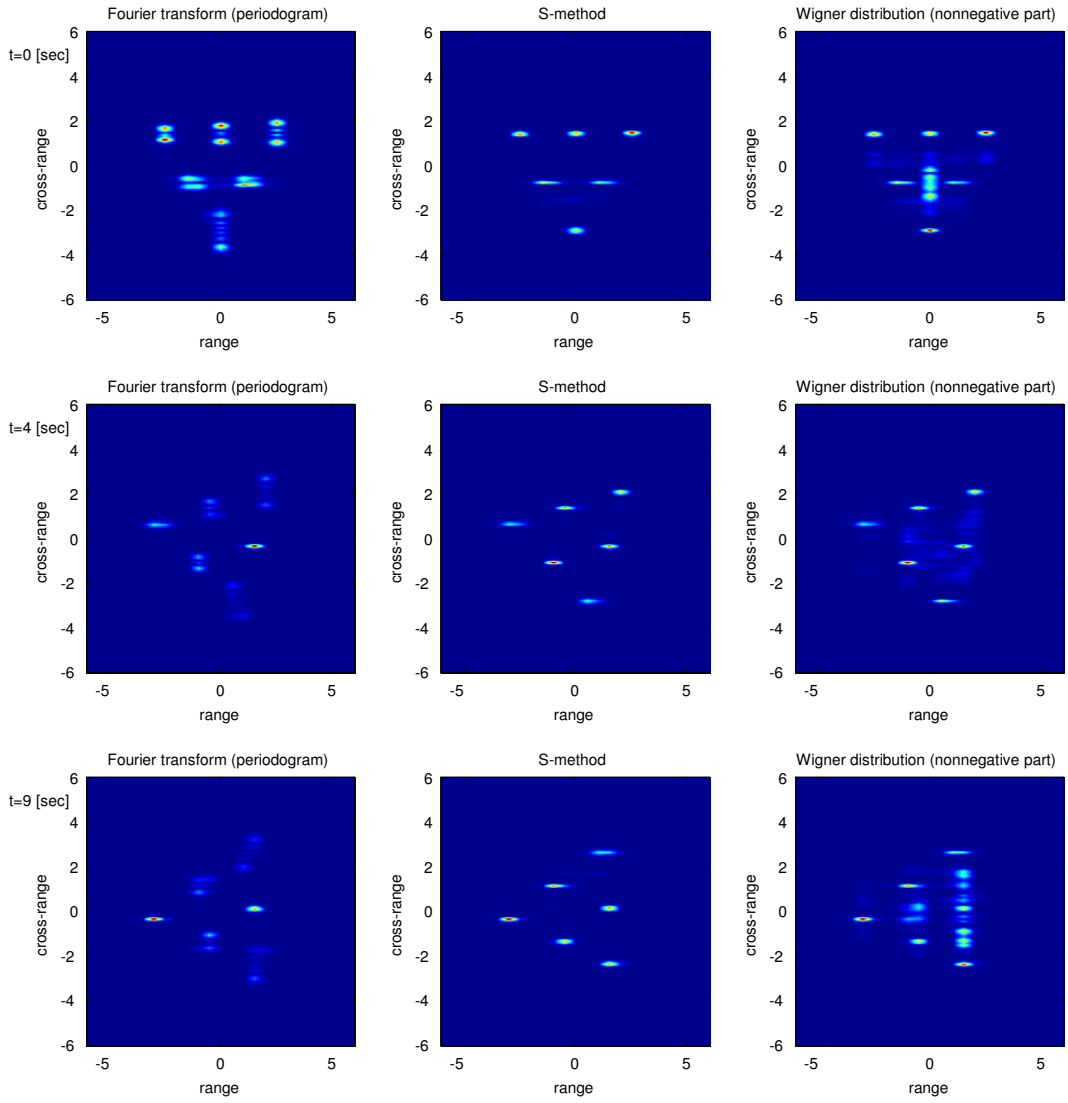

Fig. 3. ISAR images of a two-dimensional target model. Periodogram (left column), S-method (middle column), Wigner distribution (right column). Images are presented at three time instants: $t = 0$ (first row), $t = 4$ sec (second row) and $t = 9$ sec (third row).

with

$$\begin{aligned} \theta'_R(t) &= \omega_R(t) = \omega_R + A\sin(2\pi\Omega t), \\ \theta_R(t) &= \omega_R t - A/(2\pi\Omega)\cos(2\pi\Omega t) + \phi_0 \end{aligned}$$

Thus, the signal model is of the form:

$$q(m,t) = \sum_{p=1}^{6} q_p(m,t)$$

$$= \sum_{p=1}^{6} \sigma_p e^{(j\omega_0 \frac{2d_p(t)}{c})} e^{(-j2\pi B f_r (t - mT_r)\frac{2d_p(t)}{c})} \quad (18)$$

Assuming that $T_0 = 0$ and neglecting the constant phase terms with $t - mT_r = nT_s$, the model is completely defined.

The results obtained for several target positions are presented in Figure 3. The radar images presented in the range/cross-range do-

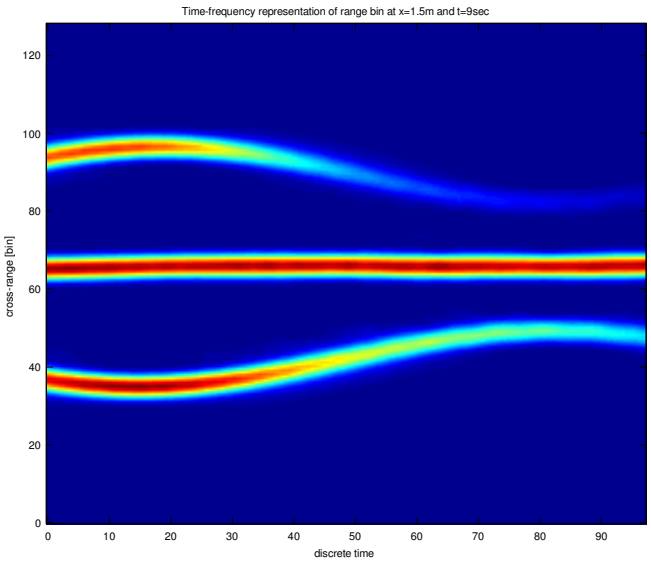

Fig. 4. Time-frequency representation of the bin at range $x = 1.5$ m and position at $t = 9$ sec.

main obtained using the Fourier transform (periodogram), the S-method and the WVD at time instants $t = 0$, 4 and 9 sec are given in this figure. In order to keep the same scale for presentation we have presented only the non-negative part of the WVD. It is known that the negative values are present in the cross-terms that do not contain information about the target, but can only degrade the image. Therefore, removing negative parts will not lose any useful information.

In order to illustrate where the cross-range spread comes from in the previous ISAR images, as an example, we considered the case at $t = 9$ sec and the range bin at $x = 1.5$ m. Distribution of the cross-range values over the considered CIT is shown in Figure 4. We can see that the middle point-scatterer is stationary in Doppler, meaning that it will be highly concentrated in the corresponding ISAR image in Figure 3 at a range value of 1.5 m. However, the remaining two point-scatterers at this range move over the cross-range, resulting in a spread in the ISAR image.

We also calculate the number of "correct points" by finding 6 largest values in the periodogram and checking if they correspond to the true target point-scatterer positions, within the margin $\pm$1m (the region $\pm$1m around the detected point is deleted by assigning zero values). The percent of correct points found in this way is given in Table 1. Note that even in the cases of very low noise and no noise, due to very high nonstationarities, target points are missed.

For the "correct points" we also calculated the MSE from the true positions. We can see that image blurring and nonstationarities caused a high deviation of "correct points" from the true ones, resulting in high MSE, which is summarized in Table 2.

For the example, $a \sim |\Delta\omega_d'(t)|$. According to (17) we conclude that the maximal value of a can be estimated as $\frac{2\omega_0}{c}\sqrt{x_p^2+y_p^2}\theta_R''(t)$. By using the coordinates of the point with maximal distance from the center of rotation $\sqrt{x_p^2+y_p^2} = 3.74$ m and the maximal value of $\theta_R''(t) = \max\{[\omega_R + A\sin(2\pi\Omega t)]'\} = 2\pi A\Omega = 0.0685$ we get $a \sim 100$. Thus, according to (16), we can expect a total MSE improvement (percent of correct points and MSE of correct points) for a point up to $SNR_{SM}/SNR_{period} = 15.9$ corresponding to the total maximal improvement $\sigma_p^4/\sigma_\varepsilon^4 = 15.9$ or $20\log_{10}(\sigma_p/\sigma_\varepsilon) = 6$ dB.

TABLE I
PERCENT OF "CORRECT POINTS" FOR VARIOUS AMOUNTS OF NOISE, σ/A_p, $SNR = 20log_{10}(A_p/\sigma)$.

σ/A_p	Periodogram (FT)	S-method	Wigner distribution
0	95.57	100	92.74
1	96.13	100	92.62
2	95.82	100	91.39
3	95.95	99.95	87.35
4	95.28	99.57	78.67
5	90.31	95.12	65.82
6	77.58	85.65	50.98
7	64.32	71.90	38.51
8	50.98	57.57	30.78

TABLE II
MSE FOR THE "CORRECT POINTS" FOR VARIOUS AMOUNTS OF NOISE, σ/A_p, $SNR = 20log_{10}(A_p/\sigma)$. RESOLUTION MSE IS 0.0218.

σ/A_p	Periodogram (FT)	S-method	Wigner distribution
0	0.1705	0.0259	0.0293
1	0.1708	0.0262	0.0276
2	0.1717	0.0264	0.0342
3	0.1707	0.0265	0.0449
4	0.1681	0.0297	0.0920
5	0.1543	0.0367	0.1713
6	0.1382	0.0457	0.2501
7	0.1365	0.0614	0.3447
8	0.1262	0.0815	0.3968

Note that the MSE in the Fourier transform based periodogram is due to the high nonstationarities and large estimation bias. It can be reduced by taking a narrower window, i.e., smaller CIT. For example, taking a 4 times smaller CIT we get MSE = 0.0265 and 100% of correct points in the periodogram for $\sigma/A_p = 0$. However for at greater noise levels, for example $\sigma/A_p = 6$, we get MSE = 0.0414, but only 65.68% of correct points, which is a significantly smaller percentage than in the periodogram with the wider window, which was 77.58%.

B.4 Application to a Three-Dimensional Target Model

Consider now the case where the target point-scatterer at a position $\vec{r}$ rotates with an arbitrarily oriented angular velocity $\vec{\omega}$, as shown in Figure 5. The angular velocity is decomposed into three axes representing oriented rotations defined by $(\omega_{rot}, \omega_{pitch}, \omega_{yaw})$. The corresponding angles of the target point are $(\theta_r(t), \theta_{pc}(t), \theta_y(t))$, where $\theta_i(t) = \int_0^t \omega_i(\tau)d\tau + \theta_i(0)$.

If $\vec{r} = (x_p, y_p, z_p)$ is the target position at $t = 0$ then at any other instant the position $\vec{r}' = (x'_p, y'_p, z'_p)$ can be determined by using the rotation three-dimensional space matrix that reads [1]

$$\vec{r}' = R_{rot}(R_{pitch}R_{yaw})\vec{r}$$

where

$$R_{pitch} = \begin{bmatrix} \cos(\theta_{pc}(t)) & 0 & -\sin(\theta_{pc}(t)) \\ 0 & 1 & 0 \\ \sin(\theta_{pc}(t)) & 0 & \cos(\theta_{pc}(t)) \end{bmatrix}$$

$$R_{yaw} = \begin{bmatrix} \cos(\theta_y(t)) & \sin(\theta_y(t)) & 0 \\ -\sin(\theta_y(t)) & \cos(\theta_y(t)) & 0 \\ 0 & 0 & 1 \end{bmatrix}$$

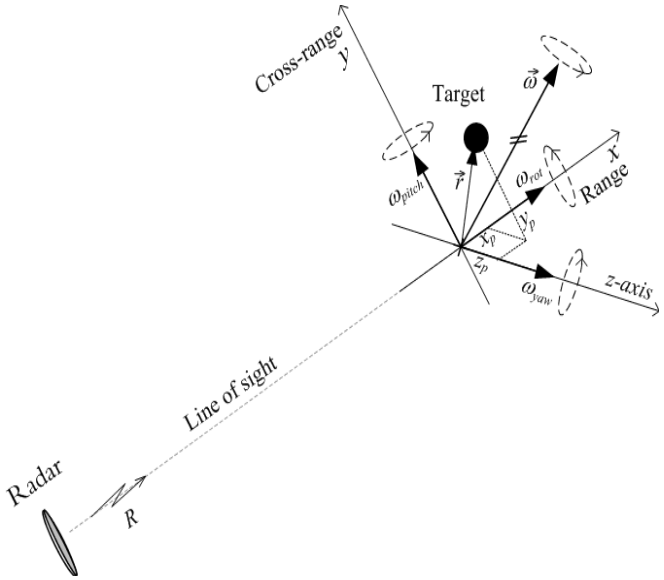

Fig. 5. The three-dimensional radar target model.

$$R_{rot} = \begin{bmatrix} 1 & 0 & 0 \\ 0 & \cos(\theta_r(t)) & \sin(\theta_r(t)) \\ 0 & -\sin(\theta_r(t)) & \cos(\theta_r(t)) \end{bmatrix}$$

or

$$\begin{bmatrix} x'_p \\ y'_p \\ z'_p \end{bmatrix} = \begin{bmatrix} a_{11} & a_{12} & a_{13} \\ a_{21} & a_{22} & a_{23} \\ a_{31} & a_{32} & a_{33} \end{bmatrix} \begin{bmatrix} x_p \\ y_p \\ z_p \end{bmatrix} \quad (19)$$

with

$a_{11} = \cos(\theta_{pc}(t))\cos(\theta_y(t))$

$a_{12} = \cos(\theta_{pc}(t))\sin(\theta_y(t))$

$a_{13} = -\sin(\theta_{pc}(t))$

$a_{21} = \sin(\theta_r(t))\sin(\theta_{pc}(t))\cos(\theta_y(t)) - \cos(\theta_r(t))\sin(\theta_y(t))$

$a_{22} = \sin(\theta_r(t))\sin(\theta_{pc}(t))\sin(\theta_y(t)) + \cos(\theta_r(t))\cos(\theta_y(t))$

$a_{23} = \sin(\theta_r(t))\cos(\theta_{pc}(t))$

$a_{31} = \cos(\theta_r(t))\sin(\theta_{pc}(t))\cos(\theta_y(t)) + \sin(\theta_r(t))\sin(\theta_y(t))$

$a_{32} = \cos(\theta_r(t))\sin(\theta_{pc}(t))\sin(\theta_y(t)) - \sin(\theta_r(t))\cos(\theta_y(t))$

$a_{33} = \cos(\theta_r(t))\cos(\theta_{pc}(t))$

Thus, in this case distance from the radar at an instant t is

$$\begin{aligned} d(t) &= \sqrt{(R(t)+x'_p)^2 + y'^2_p + z'^2_p} \\ &\cong R(t) + x'_p \\ &= R(t) + \cos(\theta_{pc}(t))\cos(\theta_y(t))x_p \\ &\quad + \cos(\theta_{pc}(t))\sin(\theta_y(t))y_p \\ &\quad - \sin(\theta_{pc}(t))z_p \end{aligned}$$

With $\theta_{pc}(t) = 0$ and $\theta_y(t) \equiv \theta_R(t)$ this model reduces to the two-dimensional model (3),(4). In general, Doppler shift and ISAR image here assume much more complex form than in the 2D case.

For small $\theta_{pc}(t)$ and $\theta_y(t)$, with $\theta_r(t) = 0$ and $R(t) = 0$, we get

$$d_p(t) \cong x_p + \theta_y(t)y_p - \theta_{pc}(t)z_p$$

$$\Delta\omega_d = \frac{2\omega_0}{c}\frac{d}{dt}[d_p(t)] \cong \theta'_y(t)\left(y_p - \frac{\theta'_{pc}(t)}{\theta'_y(t)}z_p\right).$$

Example: Consider the radar setup as in [25], [7]. Here we assume that the same dimensions and parameters are used, but with a three dimensional rotation, instead of a 2D geometry, with

$$\omega_{yaw}(t) = \omega_R(t) = \omega_R + A\sin(2\pi\Omega t)$$

$\omega_R = 6^0/\sec$, $\Omega = 0.5$ and $A = 2^0/\sec$ and $B = 600$MHz. Assume also

$$\omega_{pitch}(t) = A_{pc}\cos(2\pi\Omega_{pc}t)$$

with $A_{pc} = 3^0/\sec$, $\Omega_p = 0.25$ and the initial positions:

$(x_1, y_1, z_1) = (-2.17,\ 1.44, 1.25)$,
$(x_2, y_2, z_2) = (0,\ 1.44, 0)$,
$(x_3, y_3, z_3) = (2.17, 1.44, -1.25)$,
$(x_4, y_4, z_4) = (1.08, -0.72, -0.625)$,
$(x_5, y_5, z_5) = (-1.08, -0.72, 0.625)$ and
$(x_6, y_6, z_6) = (0, -2.89, 0)$.

All coordinates are in meters. The angle changes are:

$$\theta_y(t) = \theta_R(t)$$

$$= \omega_R t - A/(2\pi\Omega)\cos(2\pi\Omega t) + A/(2\pi\Omega)$$

$$\theta_{pc}(t) = A_{pc}/(2\pi\Omega_{pc})\sin(2\pi\Omega_{pc}t)$$

and distance compensated range is

$$d_p(t) = \cos(\theta_{pc}(t))\cos(\theta_y(t))x_p$$

$$+\cos(\theta_{pc}(t))\sin(\theta_y(t))y_p - \sin(\theta_{pc}(t))z_p.$$

The received signal is of form (18).

Results are as in the first example, including the same comments, and they are shown in Figure 6.

VI. Results and Discussion

In this section we demonstrate the application and effectiveness of the S-method as an ISAR image refocusing technique with simulated and experimental ISAR data.

A. Simulated Data:

Three numerical models were developed to simulate targets in an ISAR system.

Boeing-727 aircraft:

The first model is a Boeing 727 aircraft [1]. The simulation uses a stepped frequency X-band radar operating at a center frequency of 9 GHz. With a total of 64 stepped frequencies, the waveform has a bandwidth of 150 MHz and a range resolution of 1 m. The PRF is 20 kHz and the CIT is 0.82 seconds. A total of 64 range cells and 256 cross-range cells are used in the imaging.

This simulation makes use of a simple virtual instrument realization of the S-method, done according to (15). For L = 0, the standard Fourier transform based representation is obtained, as shown in Figure 7a. The general shape of the aircraft can be made out, but it is not possible to locate the range/cross-range cells of individual point-scatterers as they are too smeared in the cross-range dimension. By changing the number of terms, L, we get the S-method based representations with quadratic and higher-order phase errors eliminated. Figure 7b shows the refocused image with L = 3 and Figure 7c with L = 6. Compared to Figure 7a, both images show a substantial decrease in the amount of smearing in the cross-range. However, the higher L value of 6 seems to make further improvements in refocusing the nose and tail point-scatterers of the aircraft. Figure 7c is thus chosen as the best image for this data set.

MiG-25 aircraft:

The second model is a MiG-25 aircraft with 120 point-scatterers distributed along the edge of the 2D shape of the aircraft [1]. The simulation uses a stepped frequency X-band radar operating at a center frequency of 9 GHz. With a total of 64 stepped frequencies, it has a bandwidth of 512 MHz and a range resolution of 0.293 m. The PRF is 20 kHz and the CIT is 1.64 seconds. A total of 64 range cells and 512 cross-range cells are used for the imaging. The aircraft is at a range of 3,500 m and is rotating at 10 degrees/second, thus giving a cross-range resolution of about 0.058 m. The rotation rate is much higher than the normal rotation rate needed to produce a clear image of the target. We assume that target's translational motion can be perfectly compensated. However, due to the fast rotation and relatively longer image observation time, even after standard motion compensation, the uncompensated phase error is still large.

The same virtual instrument is used for MIG-25 simulation. The standard Fourier transform based representation is shown in Figure 8a. As with the Boeing-727, the general shape of the aircraft can be made out, but it is not possible to locate the range/cross-range cell of individual point-scatterers as they

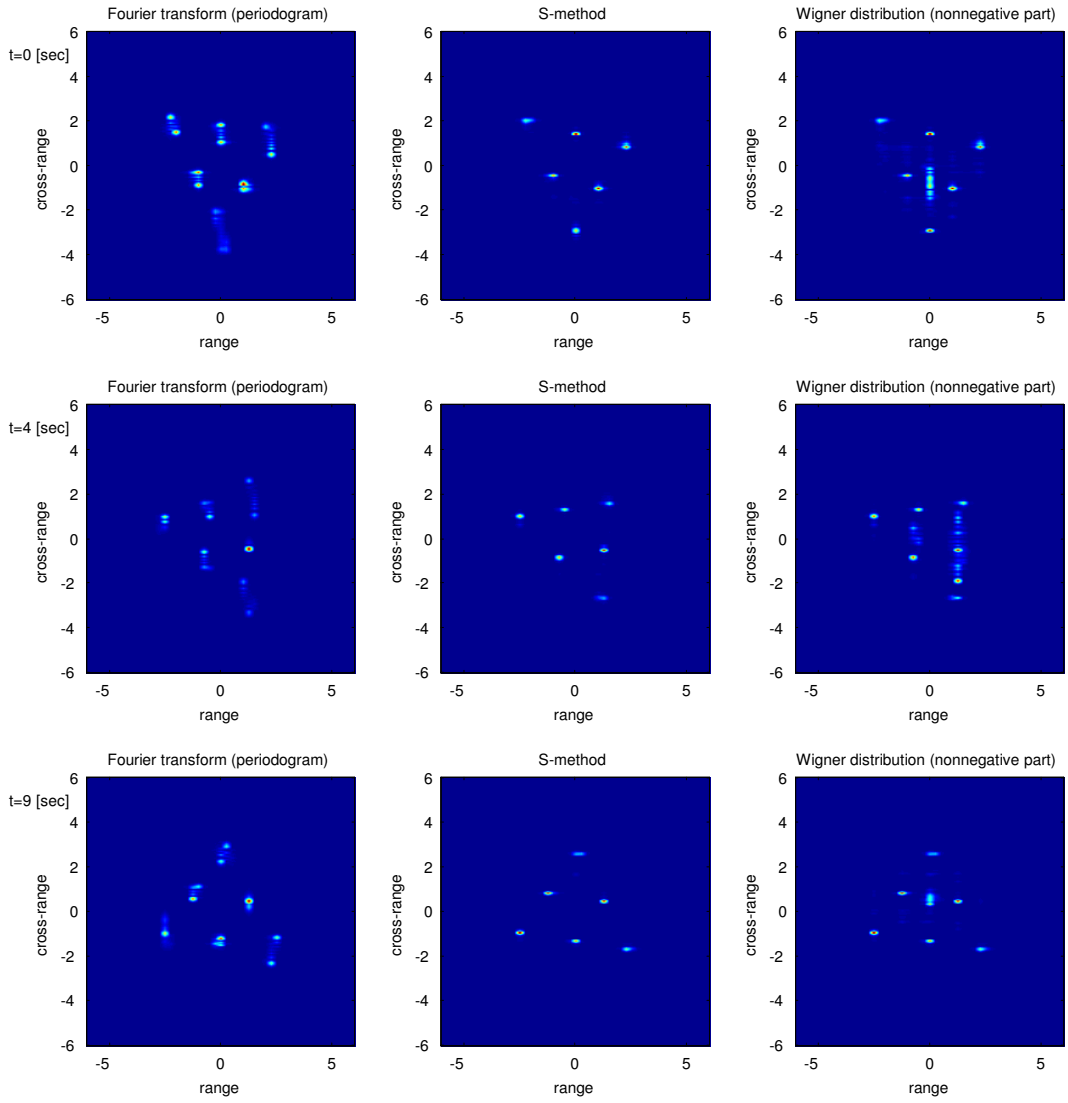

Fig. 6. ISAR images of a three-dimensional target model. Periodogram (left column), S-method (middle column), Wigner distribution (right column). Images are presented at three time instants: $t = 0$ (first row), $t = 4$ (second row) and $t = 9$ (third row).

are, once again, smeared in the cross-range dimension. The S-method representations with quadratic and higher-order phase terms eliminated are shown in Figure 8b with L = 3 and Figure 8c with L = 6. As expected, both images show a substantial improvement in the degree of smearing in the cross-range when compared to Figure 8a. The greatest improvement lies in the nose of the aircraft as it now converges to a point. However, the higher L value of 6 refocuses the nose substantially more and so Figure 8c is chosen as the best image for this data set.

F-16 aircraft:

The third and last simulation is an F-16 aircraft and was developed using a CAD model (see Acknowledgments). In this simulation, the stepped-frequency Ku-band radar is oper-

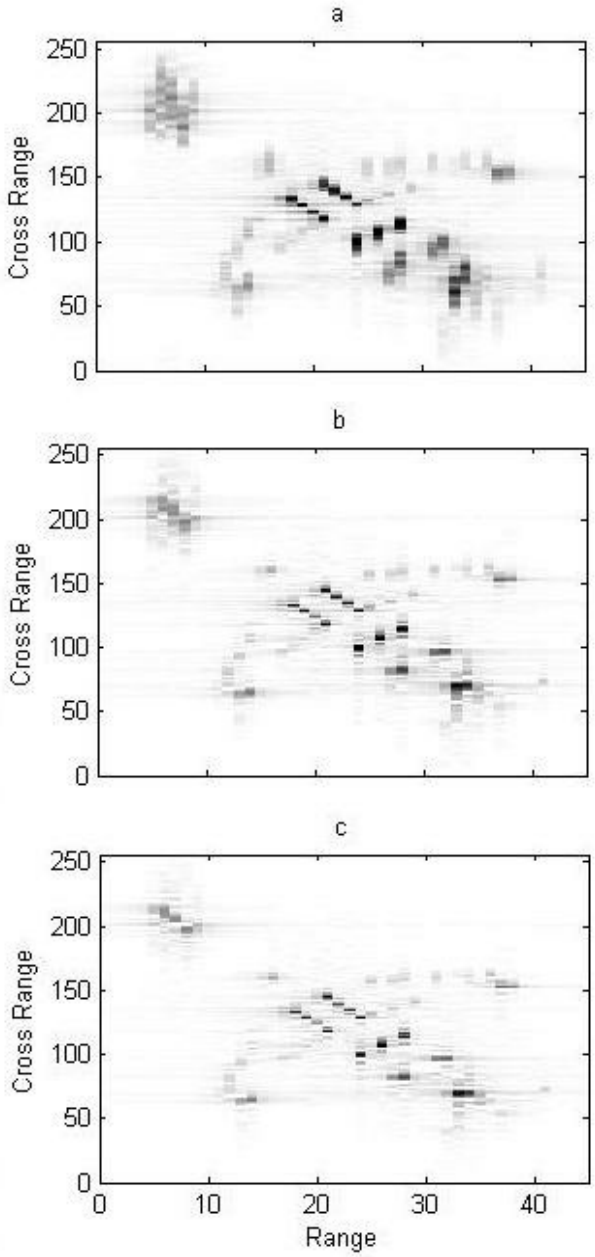

Fig. 7. ISAR images from simulated Boeing-727 data. (a) Image using conventional Fourier transform, (b) Image using the S-method with L = 3, (c) Image using the S-method with L = 6.

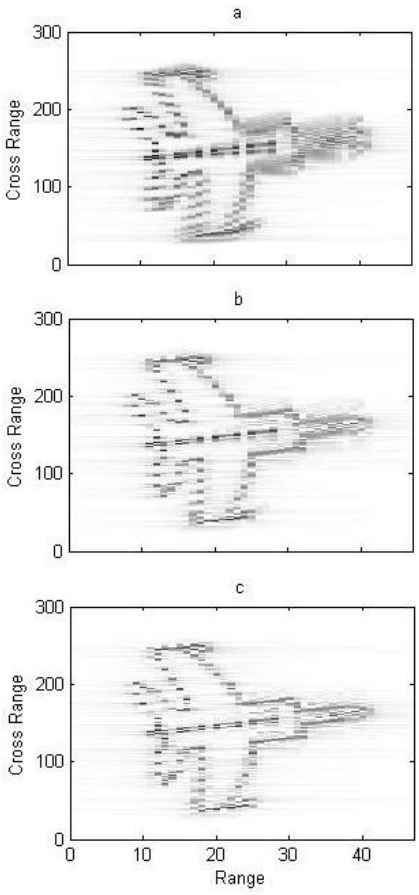

Fig. 8. ISAR images from simulated MiG-25 data. (a) Image using the conventional Fourier transform, (b) Image using the S-method with L = 3, (c) Image using the S-method with L = 6.

ating at a center frequency of 16 GHz. There are a total of 128 stepped frequencies with each step equal to 6.25 MHz, thus giving a 800 MHz bandwidth and a range resolution of about 0.188 m. A total of 91 range cells and 81 cross-range cells are used for the imaging.

Figure 9a shows the Fourier transform based representation of the F-16. The figure clearly shows that the image is severely blurred, making it impossible to identify any part of the aircraft. This means that the target's motion contains a substantial amount of rotational error. The S-method based representation, with L = 3, was selected as a suitable refocused image and is shown in Figure 9b. The S-method was able to remove most of the blurring caused by the quadratic and higher-order phase effects. However, the reflector on the wing is smeared across the entire cross-range. This is due to strong specular reflections from a few scatterers on the wing, a phenomenon caused by the CAD (computer-aided design) model rather than by jet engine modulation (JEM). Since the CAD model is composed of a large number of polygons, one such polygon's orientation in such a manner that radar returns contain specular reflection.

B. Experimental Data:

Experimental trials were conducted in an ISAR system. The data was collected from a delta-wing shaped apparatus. The delta-wing is similar to the simulated six-reflector model.

An ISAR experiment is set up to examine

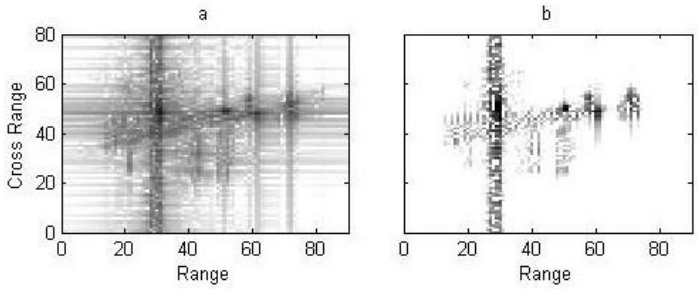

Fig. 9. ISAR images from simulated F-16 data. (a) Image using conventional Fourier transform, (b) Image using the S-method with L = 3.

Fig. 10. Picture of the delta-wing target motion simulator apparatus.

the distortion of ISAR images due to a time-varying rotational motion. A 2-dimensional delta-wing shaped target, the target motion simulator (TMS), is built for the ISAR distortion experiments. A picture of the TMS is shown in Figure 10. The target has a length of 5 m on each of its three sides. Six trihedral reflectors are mounted on the TMS as scattering centres of the target; all the scatterers are located on the x-y plane. They are designed to always face towards the radar as the TMS rotates. The TMS target is set up so that it rotates perpendicular to the radar line of sight. This simplified target geometry is identical to the one used in the numerical model given in the previous section. Note that one corner reflector is placed asymmetrically to provide a relative geometric reference of the TMS target. A time-varying rotational motion is introduced by a programmable motor drive.

The delta-wing data was collected using an X-band radar operating at a center frequency of 10.1 GHz with 300 MHz bandwidth and a range resolution of 0.5 m. The PRF is 2 kHz. Each HRR profile is generated in 0.5 ms and each profile has 41 range bins. The total data set contains 60,000 HRR profiles. The delta-wing is at a range of 2 km and is rotating at 2 degrees/second.

Since the entire data set consists of 60,000 pulses in the cross-range, it can be "cut" into different size imaging intervals with each of the

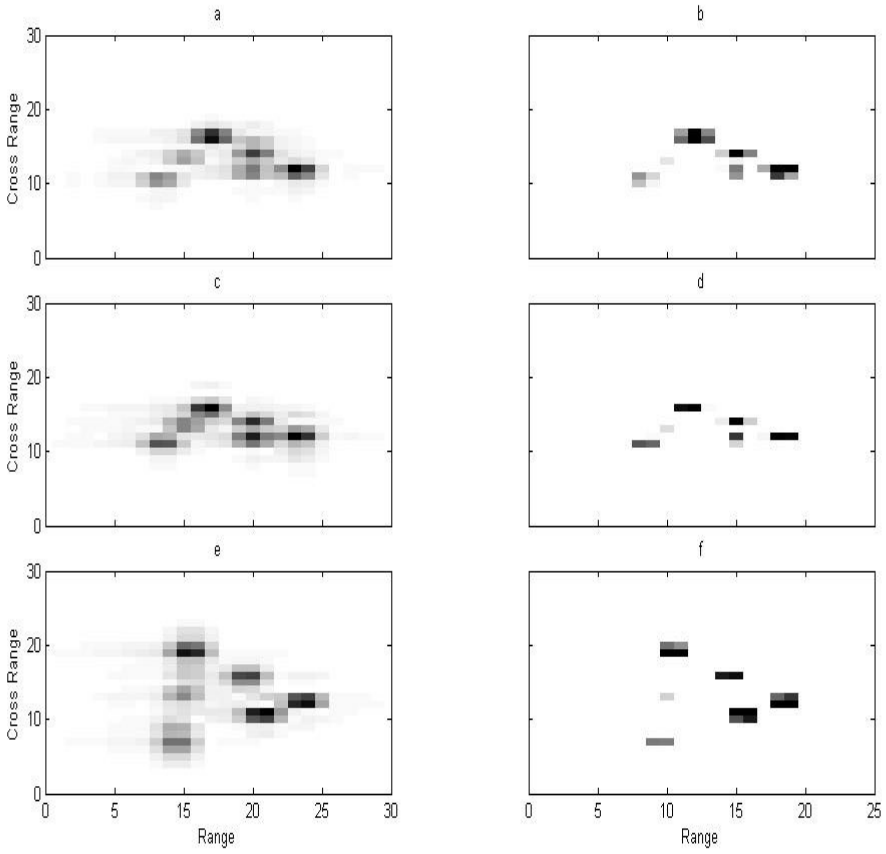

Fig. 11. ISAR images from experimental delta-wing data. First column contains Fourier transform based images and second column contains S-method based ISAR images. Each image is zoomed in on the target for clear presentation.

intervals displaying a different amount of motion error. This is the approach used in this paper. Figures 11-13 show ISAR images from three different imaging intervals. The smallest interval consists of 1024 pulses in the cross-range, which corresponds to a CIT of 0.512 seconds (Figure 11) and the largest interval consists of 4096 pulses, which corresponds to 2.048 seconds (Figure 13). Figure 12 shows the ISAR image from 2048 pulses, which corresponds to a CIT of 1.024 seconds. The Figures' leftmost columns show the Fourier transform based representations and their rightmost columns show the S-method based representations. Since significant phase errors due to nonuniform motion exist in the data, the Fourier transform based images are blurred in the cross-range dimension. This is most evident in Figures 13a, 13c, 13e and 12a where it is not possible to locate individual reflectors as some are severely blurred. In each of the S-method based images, the cross-range smearing is significantly reduced resulting in a dramatic improvement in image quality. The images are now focused and the six reflectors are visible.

When compared to the simulated six reflector images, it is clear that the experimental images in Figures 11-13 are less focused. This is mainly due to angular dependencies between radar and target, and shadowing effects that corrupt the radar return.

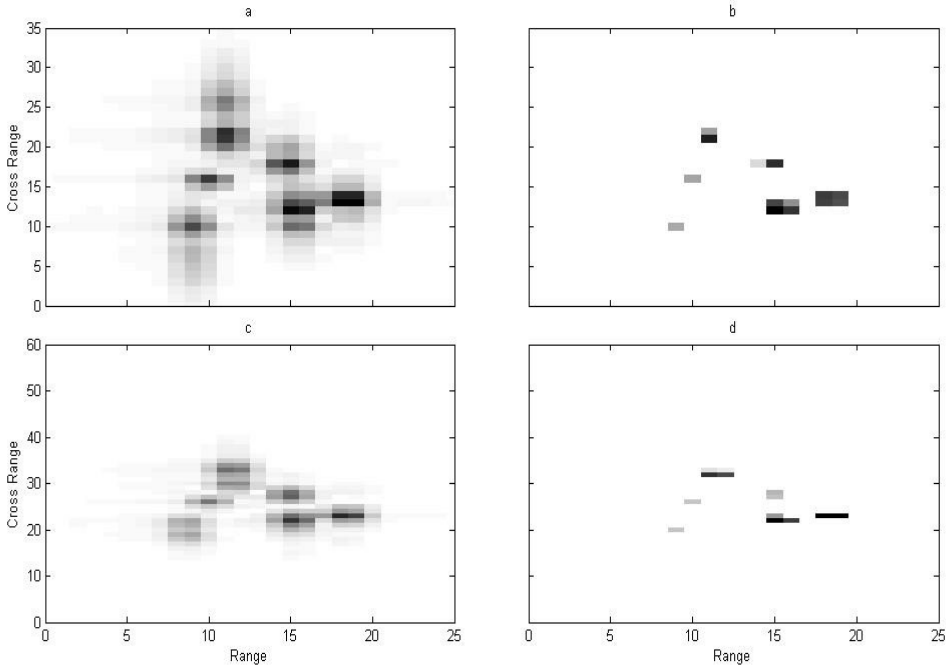

Fig. 12. ISAR images from experimental delta-wing data. First column contains Fourier transform based images and second column contains S-method based ISAR images. Each image is zoomed in on the target for clear presentation.

The amount of time it took the Fourier transform and S-method program codes to be executed was measured for each of the above data sets. The program codes were executed in Matlab using a Pentium-IV 2.66 GHz with 2.1 Gbyte of RAM. In relation to the Fourier transform, the S-method ran 1.5 to 5.5 times more slowly correspond to L values of 1 and 7, respectively. Each L value in the range 1 to 7 was used in producing refocused images of the above data sets. When compared to other transforms, the S-method performs faster. The WVD was applied to the above data sets. This gave an average processing time that is 592 times slower than the Fourier transform, and significantly slower than the S-method. The results indicate that the S-method is able to produce well focused images in real-time. For this reason, it is a useful technique for detecting targets.

VII. Conclusion

In this paper, we present the S-method based approach to real-time motion compensation, image formation and image enhancement of moving targets in ISAR and SAR. This approach performs better than the Fourier transform by drastically improving images of fast, maneuvering targets by increasing the SNR in both low and high noise environments. These advantages are a result of the S-method's ability to automatically compensate for quadratic and all even higher-order terms in phase. Thus, targets with constant acceleration will undergo full motion compensation and their point-scatterers will each be localized. It should be noted that the source of the quadratic term can come from not only acceleration, but also non-uniform rotational motion and the cosine term in wide-angle imaging. The method is also computationally simple, requiring only slight modifications to the existing Fourier transform based algorithm.

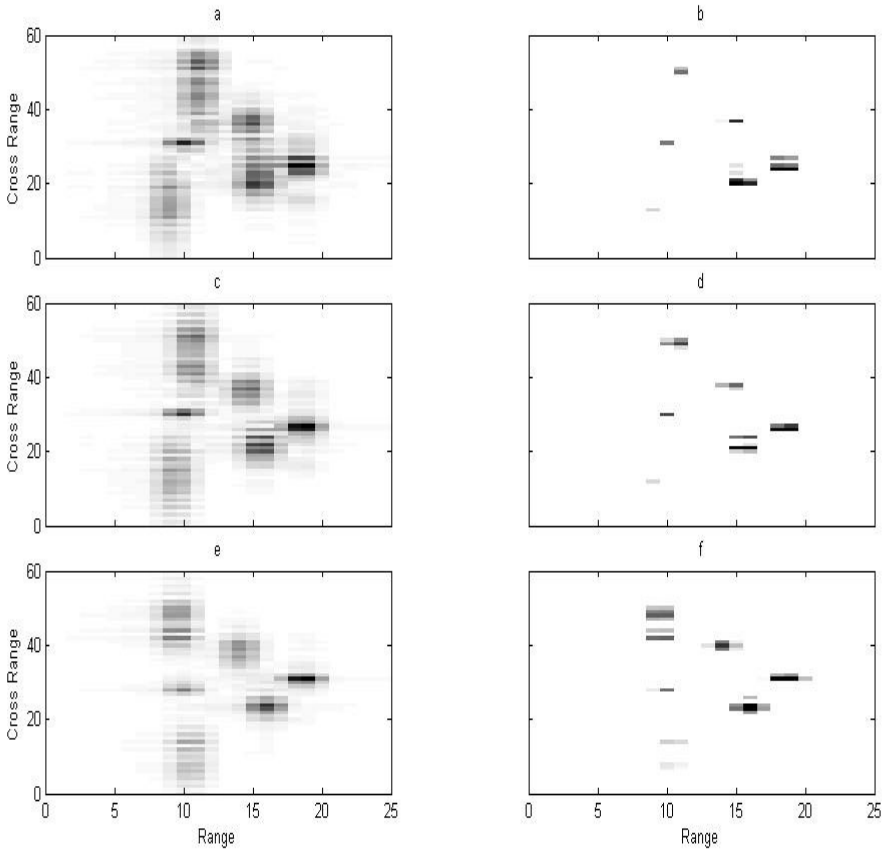

Fig. 13. ISAR images from experimental delta-wing data. First column contains Fourier transform based images and second column contains S-method based ISAR images. Each image is zoomed in on the target for clear presentation.

The effectiveness and robustness of the S-method is made evident through an analysis of its performance with noisy signals. It is shown to increase the SNR in both low and high noise environments, thereby improving images in essentially all situations. A formula is derived for the ratio of the S-method SNR to the Fourier transform SNR, and confirms the advantage of using the S-method in cases of non-stationary signals. The S-method's performance with targets exhibiting three-dimensional motion is also presented. Such motion is among the many used in simulated and experimental data sets to which the S-method is applied. These data sets are range from groups of microwave reflectors rotating in a two-dimensional plane to fast-maneuvering aircraft exhibiting complex changes in pitch, roll, and yaw. In all cases, while the Fourier transform produces images with severe blurring, the S-method is able to produce focused images of the targets by locating prominent point-scatterers in their respective range and cross-range cells. Results indicate that the S-method greatly surpasses the conventional Fourier transform method in improving blurred and distorted ISAR images due to various target motions. The comparisons also made it clear that the S-method is computationally efficient, as its algorithm is executed in little as 1.5 times slower than the conventional Fourier transform's.

This paper demonstrates that the S-method

can be applied to real-time target identification in ISAR systems. This work is especially pertinent to the ISAR imaging capability in military intelligence, surveillance and reconnaissance operations.

Acknowledgments

We would like to thank Silvester Wong (DRDC Ottawa) for supplying us with the simulated F-16 data.

References

[1] Chen, V. C. and Ling, H. (2002). Time-frequency transforms for radar imaging and signal analysis, *Artech House,* Boston, USA.

[2] Wehner, D. (1987). High Resolution Radar, *Artech House,* Boston, USA.

[3] Chen, C. C. (1980). Target-motion-induced radar imaging, *IEEE Trans. Aero. and Electronic. Sys.,* AES-16, No. l, pp. 2-14.

[4] Walker, J. L. (1980). Range-Doppler imaging of rotating objects, *IEEE Trans. Aero. and Eletronic. Sys.,* AES-16, No. l, pp. 23-52.

[5] Sparr, T., Hamran, S-E., and Korsbakken, E. (2000) Estimation and correction of complex target motion effects in Inverse Synthetic Aperture imaging of aircraft, *IEEE International Radar Conference,* pp. 457-461, Alexandria USA.

[6] Wang, Y., Ling, H., and Chen, V. C. (1998). ISAR motion compensation via adaptive joint time-frequency techniques, *IEEE Trans. Aerospace and Electronics Systems*, 34, pp. 670-677.

[7] Thayaparan, T., Lampropoulos, G., Wong, S. K., and Riseborough, E. (2003). Application of adaptive joint time-frequency algorithm for focusing distorted ISAR images from simulated and measured radar data, *IEE Proc. Radar, Sonar Navig.,* Vol. 150, No. 4, pp. 213-220.

[8] Cohen, L. (1995). Time-frequency analysis, *Prentice-Hall Inc.,* New York, USA.

[9] Thayaparan, T. and Kennedy, S. (2004). Detection of a manoeuvring air target in sea-clutter using joint timefrequency analysis techniques, *IEE Proc.-Radar Sonar Navig.,* vol. 151, No. 1, pp. 19-30.

[10] Qian, S. and Chen, D. (1996). Joint time-frequency analysis: methods and applications, *Prentice-Hall Inc.,* New York, USA.

[11] Wong, S. K., Riseborough, E., and Duff, G. (2006). An analysis of ISAR image distortion based on the phase modulation effect, *EURASIP J. on appl. Sig. Processing,* pp. 1-16.

[12] Stankovic, L., Thayaparan, T., and Dakovic, M. (2006). Improvement of the fast moving targets presentation in ISAR by using the S-Method, September 4-8, 2006, Florence, Italy.

[13] Thayaparan, T., Stankovic, L., and Dakovic, M. (2006), Focusing distorted ISAR images using the s-method, pp. 121-125, May 7, IEEE CCECE 2006 Conference, Ottawa, Canada.

[14] Thayaparan, T., Stanković, L. J., C. Wernik., and Daković, M. (2001). A Novel S-Method-Based Approach for Real-Time Motion Compensation, Image Formation and Image Enhancement of Moving Targets in ISAR and SAR, *DRDC Ottawa TR 2006-246,* Defence R&D Canada - Ottawa, Canada.

[15] Stanković, L. J. (1996). The auto-term representation by the reduced interference distributions: The procedure for a kernel design, *IEEE Trans.on Signal Processing*, Vol. 44, No. 6, pp. 1,557-1,564.

[16] Stanković, L. J. (1994). A method for time-frequency analysis, *IEEE Trans. Signal Process.*, Vol. 42, pp. 225-229.

[17] Stanković, L. J. and Böhme, J. F. B. (1999). Time-frequency analysis of multiple resonances in combustion engine signals, *Signal Processing,* Vol. 79, No. 1, pp. 15-28.

[18] Scharf, L. L. and Friedlander, B. (2001). Toeplitz and Hankel kernels for estimating time-varying spectra of discrete-time random processes, *IEEE Trans. Signal Process.*, Vol. 49, pp. 179-189.

[19] Boashash, B. (1992). Estimating and interpreting the instantaneous frequency of a signal Part 1, *IEEE Proc.*, Vol. 80, No. 4, pp. 519-538.

[20] Papoulis, A. (1977). Signal analysis, *McGraw Hill Book Company,* New York, 1977.

[21] Stanković, L. J., Daković, M., and Ivanović, V. (2001). Performance of spectrogram as IF estimator, *Electronics Letters,* Vol. 37, No. 12, pp. 797-799.

[22] Ivanović, V. N., Daković, M., and Stanković, L. J. (2003). Performance of quadratic time-frequency distributions as instantaneous frequency estimators, *IEEE Trans.on Signal Processing*, Vol. 51, No. 1, pp. 77-89.

[23] Stanković, L. J., Ivanović, V., and Petrović, Z. (1996). Unified approach to the noise analysis in the Wigner distribution and Spectrogram, *Annales Telecomm.,* pp. 585-594.

[24] Richard, C. (2002). Time-frequency-based detection using discrete-time discrete-frequency Wigner distributions, *IEEE Trans. on Signal Processing*, Vol. 50, No. 9, pp. 2,170-2,176.

[25] Wong, S. K., Duff, G., Riseborough, E., (2006). Distortion in the inverse synthetic aperture radar (ISAR) images of a target with time-varying perturbed motion, IEE Proc.-Radar Sonar Navig., Vol. 150, No. 4, pp. 221-227.